



Article

Harmonic Analysis of Sliding-Mode-Controlled Buck Converters Imposed by Unmodeled Dynamics of Hall Sensor

Yanmin Wang ^{1,*} , Guangxin Duan ¹ , Juan Yu ², Wenjiao Yue ², Jiaming Ning ¹ and Bailiang Liu ¹

¹ School of Electrical Engineering and Automation, Harbin Institute of Technology, Harbin 150001, China; 22s006052@stu.hit.edu.cn (G.D.); 18847047599@163.com (J.N.); mingzhi94814@163.com (B.L.)

² Yatai Construction Science & Technology Consulting Institute Co., Ltd., Beijing 100120, China; yujuan2006708@126.com (J.Y.); yuezijiao@yeah.net (W.Y.)

* Correspondence: wangyanmin@hit.edu.cn

Abstract: DC–DC buck converters have become prominent components for energy optimization in power systems, and how to improve control performances is a challenging issue to be addressed. In this paper, we aim to investigate the harmonic problem of sliding mode (SM) controlled buck converters imposed by the often-ignored unmodeled dynamics of the Hall sensor. The unified mathematical model of the whole system is established by combining the SM controller, the buck converter, and the Hall sensor, where the signal loss in the transmission process of the whole closed-loop control system is considered. Based on the Lyapunov stability theorem, the SM controller is designed to guarantee system stability, as well as to deduce the stable working areas and the tuned controller parameters. Furthermore, we introduce the descriptive function (DF) approach to investigate the influence of the unmodeled dynamics of the Hall sensor on the system harmonics in the frequency domain, which can deduce the relationship between the amplitude-frequency characteristics of the output signal and the Hall sensor. Simulations and experiments validate this paper.

Keywords: sliding mode control; DC–DC converter; harmonic analysis; unmodeled dynamics; descriptive function approach; frequency analysis



Citation: Wang, Y.; Duan, G.; Yu, J.; Yue, W.; Ning, J.; Liu, B. Harmonic Analysis of Sliding-Mode-Controlled Buck Converters Imposed by Unmodeled Dynamics of Hall Sensor. *Energies* **2023**, *16*, 6124. <https://doi.org/10.3390/en16176124>

Academic Editor: Abu-Siada Ahmed

Received: 23 July 2023

Revised: 18 August 2023

Accepted: 19 August 2023

Published: 22 August 2023



Copyright: © 2023 by the authors. Licensee MDPI, Basel, Switzerland. This article is an open access article distributed under the terms and conditions of the Creative Commons Attribution (CC BY) license (<https://creativecommons.org/licenses/by/4.0/>).

1. Introduction

With the rapid development of new energy, distributed power systems, and the wide use of uninterrupted power systems (UPS), DC–DC buck converters have played an important role in energy optimization. How to improve its conversion efficiency and performance is an important but challenging issue to be considered [1,2]. It is a well-known fact that DC–DC buck converters are a typical class of nonlinear systems due to the contained nonlinear circuit components such as the capacitors, inductors, switches, and the external disturbances imposed by the possible measurement sensors, the signal loss in the transmission process and some unmodeled dynamics [3,4], which are often ignored in modeling and controlling. However, it is worth noticing that all these factors can reduce the performance of the buck converters, or even lead to instability.

An appropriate control approach has a significant function to realize better performances. Compared with the traditional control approaches such as PI and linear feedback control, sliding mode (SM) control is characterized by nonlinear and robust control due to its contained switching function $\text{sgn}(\cdot)$. Much research found in the literature has proved that SM control is more suitable for the switching control of buck converters; a review of recent SM applications in power converters can be found in [5]. On the one side, SM is inherently nonlinear and differs from the approximate nonlinearity of the substitutes as fuzzy control [6,7], neural network [8,9], and other intelligent control approaches [10–12]. Therefore, the control performances under SM control are better; furthermore, the amount

and time of the calculation can also be saved. On the other side, thanks to its natural switching control property, the SM controller can replace the traditional pulse-width modulation (PWM) and realize the direct ON/OFF switching control of the converters by triggering the gate of the controllable power switches. As a result, it is simple and no extra modulation circuits are needed [13,14]. At present, various types of SM have been applied for the control of buck converters, including linear sliding mode (LSM), terminal sliding mode (TSM), and non-singular terminal sliding mode (NTSMC). For example, in [15], an LSM controller was proposed to realize the asymptotic convergence of the output voltage; in [16], a TSM controller was designed to improve the steady accuracy and response speed due to its finite-time convergence; in [17], an NTSMC controller was proposed to realize the wide-range voltage regulation of the buck converters due to its global finite-time convergence. Attention should be paid to the fact that the design of SM controllers is commonly focused on the stability in the time domain, and it is difficult to investigate the control performances in the frequency domain [18–21], especially for the harmonics, which is a key performance index in the practical applications of buck converters.

In this paper, the harmonic analysis of SM-controlled buck converters is carried out in frequency. Compared with the time-domain analysis based on the Lyapunov stability theorem, frequency-domain analysis is based on the Fourier transform and can make it easier to obtain the detailed information of the concerned signals [22–25], including the visual representation and the corresponding values of the amplitude and frequency. At present, the Poincaré map and descriptive function are the two main approaches adopted in frequency-domain analysis. For example, in [22], the Poincaré map and linear matrix were combined to investigate the stability and the periodic solutions for a class of relay systems, and then in [23], the Poincaré map was applied in an SM control system to analyze its inherent chattering phenomenon, proving the fact that the control nonlinearity of SM can induce harmonics in practical systems. In [24], the descriptive function (DF) was adopted to analyze the frequency characteristics of DC–DC converters. Compared with the Poincaré map, DF is easier to implement and more suitable for practical systems. The idea of DF is to utilize the characteristic curves of the amplitude, phase, and frequency to visually observe the performance of the system, following the improvement by adjusting the controller parameters. In [25], a boost converter was taken as an example to solve the problem of switch linearization by utilizing DF; in [26], the two problems of the stability and limit cycle were investigated for a class of LSM-controlled uncertain system, and further deduced the relationship between parameter uncertainties, the position, and distribution characteristics of zeros and poles. All of these show the effectiveness of DF approaches applied in SM-controlled systems.

Unmodeled dynamics commonly exist in practical systems, which usually originate from sensors, actuators, and higher-order state terms. They are generally unmeasurable and characterized by small time constants, so that they are often ignored in modelling and controlling. Some of the literature concerning the overcoming and observation of unmodeled dynamics can be found in [27]. In this paper, the influence of the often-ignored unmodeled dynamics of the Hall sensor on SM-controlled buck converter systems is another challenging issue to be addressed. In practical circuits, various Hall sensors, such as ACS712 (<https://www.alldatasheet.com/datasheet-pdf/pdf/168326/ALLEGRO/ACS712.h-tml>, accessed on 18 August 2023), ACS706 (<https://www.alldatasheet.com/datasheet-pdf/pdf/174113/ALLEGRO/ACS-706ELC-05C.html>, accessed on 18 August 2023) and ACS758 (<https://www.alldatasheet.com/datasheet-pdf/pdf/53346-8/ALLEGRO/ACS758.html>, accessed on 18 August 2023) are generally used to measure currents, which can be further adopted for the design of controllers. The idea of Hall sensors is based on the Hall effect, which can realize contactless current measurement [28]. Furthermore, it can prioritize the safety of both individuals and equipment, and maintains the structural integrity of the original circuit, whereby the measurement accuracy can be improved. At present, if the Hall sensor is used in an open-loop control system, its measurement error can be less than 1%, while if it is used in a closed-loop control system, the measurement error can be less

than 0.2% [29]. Due to the high accuracy of Hall sensors, the signal loss in the transmission process is often ignored. However, the model of the Hall sensor can be categorized as the unmodeled dynamics in the sense of control, which are characterized by rapidity and/or small scale and are generally described as a first-order or second-order transfer function [30]. In practice, the unmodeled dynamics are caused by system complexity, model inaccuracy, and measurement errors. Furthermore, in [31], it has been proved that the influence of unmodeled dynamics can not be avoided, especially in SM control systems. Since the system order is increased artificially by introducing the unmodeled dynamics, the chattering problem (called the harmonic problem in real systems) occurs due to the contained switching function $\text{sgn}(\cdot)$, which can reduce the dynamic and static performances or even destroy the system stability [11,32].

In order to overcome the influence of unmodeled dynamics, much of the literature is mainly concentrated on observation and compensation, seen for example in [33–35]. In [33], an adaptive neural network control approach is adopted for the information recognition of the unmodeled dynamics of the actuator. In [34], the unmodeled dynamics caused by the nonideal constant power loads were considered and their information was achieved by designing an SM observer. In [35], a second-order SM controller was designed to compensate for the influence of unmodeled dynamics and external disturbances, where the upper boundary was only needed. However, how the unmodeled dynamics affect the performance index, especially in the frequency domain, is seldom studied.

In this paper, the harmonic problem of SM-controlled buck converters imposed by the often-ignored unmodeled dynamics of the Hall sensor is investigated. The unified mathematical model of the SM controller, the buck converter, and the Hall sensor is established. The stability in the time domain and frequency domain is investigated and compared based on the Lyapunov stability theorem and Nyquist stability criterion, respectively. Furthermore, by utilizing the DF approach, the relationship between the amplitude and frequency of the output signal can be deduced for the SM-controlled buck converter system. To be specific, the main contributions of this paper can be summarized as follows:

- The unified mathematical model of the whole system is established by combining the SM controller, the buck converter, and the Hall sensor, and the signal loss caused by the non-ideal Hall sensor is considered;
- Investigations of the stability and the tuning range of the SM controller are carried out in the time domain and frequency domain for comparison;
- By utilizing the DF approach, the harmonics induced by the sensor unmodeled dynamics can be proved;
- The relationship between the amplitude frequency characteristics of the output signal and the Hall sensor is determined.

This paper is organized as follows. In Section 2, the SM-controlled buck converter is described, including the description of the buck converter and the Hall sensor, and the design of the SM controller based on Lyapunov stability in the time domain. In Section 3, the stability analysis in the frequency domain is carried out by utilizing the DF approach and Nyquist stability criterion. In Section 4, the influence of the sensor's unmodeled dynamics on the harmonics is investigated quantitatively. Finally, the simulations, experiments, and concluding remarks are given in Sections 5 and 6, respectively.

2. System Description and Modelling

In Figure 1, the system diagram of an SM-controlled buck converter is given [15–21], which is composed of three parts, i.e., the buck converter, SM controller, and Hall sensor. Where E is the input DC voltage source, S_w is a controllable power switch (N-MOSFET is often adopted), and its ON/OFF is controlled by the output signal u of the SM controller; VD is a continuity diode, and the types of fast recovery diode or Schottky diode are often selected; L and C are the filter inductor and capacitor, respectively, and v_L is the voltage of inductor L ; i_L , and i_C are the currents flowing through L and C ; R is the load resistor, and

v_C is the output voltage and can be achieved by using voltage divider resistor R_1 and R_2 with ration $\beta = R_1/(R_1 + R_2)$.

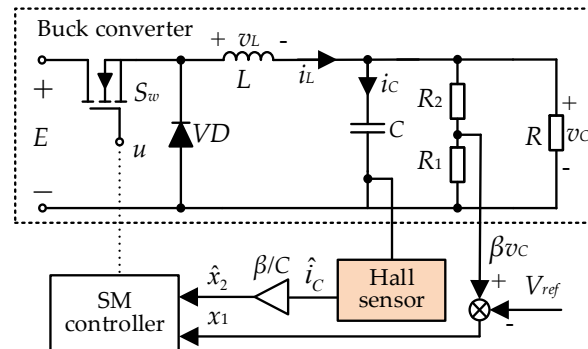


Figure 1. Diagram of the SM-controlled buck converter system.

In practice, it is known that the current i_C is usually measured by the Hall sensor, but is often ignored. However, its influence on the control system should be ignored, as seen in the literature [27–32]. Therefore, this paper innovatively considers it in modelling and controlling. In the following, the description of the buck converter, the Hall sensor, and the design of the SM controller is given.

2.1. Buck Converter

In this paper, the buck converter is assumed to work in continuous conduction mode (CCM), i.e., $i_L > 0$. Based on the structural characteristics of the converter, the differential equation describing its ON/OFF operation can be given as [15]

$$\begin{cases} \frac{di_L}{dt} = -\frac{1}{L}v_C + \frac{E}{L}u \\ \frac{dv_C}{dt} = \frac{1}{C}i_L - \frac{1}{R_0C}v_C \end{cases} \quad (1)$$

where $\{0, 1\}$ is the output pulse of the controller, $R_0 = R(R_1 + R_2)/(R + R_1 + R_2)$.

If we take the second derivative of the variable v_C , and substitute the term of di_L/dt in (1) into it, the dynamics of the output voltage can be rewritten as a second-order differential equation as

$$\ddot{v}_C + \frac{1}{R_0C}\dot{v}_C + \frac{1}{LC}v_C = \frac{uE}{LC} \quad (2)$$

Furthermore, we define V_{ref} as the DC reference value of the output voltage v_C ; x_1 and x_2 are the output voltage error and its derivative, i.e.,

$$\begin{cases} x_1 = \beta v_C - V_{ref} \\ x_2 = \dot{x}_1 = \beta \dot{v}_C \end{cases} \quad (3)$$

By combining (2), (3) can be changed into the state space form as

$$\dot{x} = Ax + bu + f \quad (4)$$

where the state vector $x = [x_1, x_2]^T$, the matrix A , b , and f are listed as

$$A = \begin{bmatrix} 0 & 1 \\ -\frac{1}{LC} & -\frac{1}{R_0C} \end{bmatrix}, \quad b = \begin{bmatrix} 0 \\ \frac{\beta E}{LC} \end{bmatrix}, \quad f = \begin{bmatrix} 0 \\ -\frac{V_{ref}}{LC} \end{bmatrix}$$

2.2. Hall Sensor

In this paper, the signal loss of the Hall sensor located in the converter circuit is considered, as seen in Figure 1, i.e., $i_C \neq \hat{i}_C$, $x_2 \neq \hat{x}_2$, where \hat{i}_C and \hat{x}_2 are the measured

values corresponding to the variables i_C and x_2 . Meanwhile, the transmission characteristics of the Hall sensor are taken into account. Based on the sensor theory, the unmodeled dynamics of the Hall sensor can be expressed as a standard second-order system as [36]

$$\ddot{\hat{i}}_C + 2\zeta\omega_n\dot{\hat{i}}_C + \omega_n^2\hat{i}_C = K\omega_n^2i_C \quad (5)$$

where i_C and \hat{i}_C are the input and output of the Hall sensor, respectively; ω_n is the angular frequency, K is the amplification coefficient, and the damp ratio $0 < \zeta < 1$.

From (5), the transfer function $G_h(s)$ of the Hall sensor can be accordingly deduced in terms of the Laplace transformation as

$$G_h(s) = \frac{K\omega_n^2}{s^2 + 2\zeta\omega_n s + \omega_n^2} \quad (6)$$

The step response $c(t)$ of the Hall sensor can also be expressed as

$$c(t) = K - \frac{K}{\sqrt{1-\zeta^2}} e^{-\zeta\omega_n t} \sin\left(\omega_n \sqrt{1-\zeta^2} t + \arccos\zeta\right) \quad (7)$$

Therefore, the rise time ψ can be obtained from (5) as

$$\psi = \frac{\pi - \arccos\zeta}{\omega_n \sqrt{1-\zeta^2}} \quad (8)$$

By combining Figure 1 and (1) in the frame of Kirchhoff's circuit law, there is $i_c = C\dot{v}_C$ and $\hat{x}_2 = \hat{i}_C\beta/C$. By defining $\hat{x} = [\hat{x}_2, \hat{x}_2]^T$ as the measured state vector, (5) can be changed as

$$\dot{\hat{x}} = C\hat{x} + Dx_2 \quad (9)$$

where the matrix C and D are denoted as

$$C = \begin{bmatrix} 0 & 1 \\ -\omega_n^2 & -2\zeta\omega_n \end{bmatrix}, D = \begin{bmatrix} 0 \\ K\omega_n^2 \end{bmatrix}$$

2.3. SM Controller

Much of the literature has proved the effectiveness of SM applied for the control of converters by replacing the traditional PWM approach [13,14]. At present, various types of SM approaches have been utilized, as seen in the recent survey in [5]. In this paper, we take LSM as an example to design an SM controller in Figure 1. In practice, LSM is the most widely used type due to its easy implementation. Based on the principle of the SM controller, its design includes an SM surface and a robust switching control law [15].

In this paper, the sliding surface s_L can be designed as the linear combination of the variables x_1 and \hat{x}_2 as

$$s_L = \lambda x_1 + \hat{x}_2 \quad (10)$$

where the design parameter $\lambda > 0$ and $c = [\lambda, 1]$. From Figure 1, it is worth noticing that the measured signal \hat{x}_2 is adopted directly for the controller design, where $\hat{x}_2 = \hat{i}_C\beta/C$. By combining (3), it can be seen that the crucial role of the Hall sensor is to measure the capacitor current i_C for constructing the SM controller, so that its measurement accuracy affects the control performance of the system.

For the robust switching control law, it is designed to trigger the gate pole of the controllable N-MOSFET S_w in Figure 1 as

$$u = -0.5[\text{sgn}(s_L) - 1] \quad (11)$$

The power switch driven by the control u exhibits two states, i.e., ON ($u = 1$) and OFF ($u = 0$). In other words, (11) can be described as

$$u = \begin{cases} 1 = \text{'ON'} & \text{when } s_L < 0 \\ 0 = \text{'OFF'} & \text{when } s_L > 0 \end{cases} \quad (12)$$

In order to investigate the influence of the unmodeled dynamics of the Hall sensor on the system stability, we first give the traditional SM controller design based on the time-domain stability. Meanwhile, we temporarily assume the transmission characteristics of the Hall sensor are ideal for performance comparison later, i.e., $x_2 = \hat{x}_2$. Therefore, based on the Lyapunov stability theorem, the condition $s_L \dot{s}_L < 0$ should be satisfied [15]. By combining (1) and (10), there is

$$s_L \dot{s}_L = s_L \left[\left(\lambda - \frac{1}{R_0 C} \right) x_2 + \frac{1}{LC} (\beta E u - V_{ref} - x_1) \right] < 0 \quad (13)$$

According to the two statuses of the power switch in (12), the stability condition in (13) can be changed as

$$\begin{cases} l_1 : \left(\lambda - \frac{1}{R_0 C} \right) x_2 + \frac{1}{LC} (\beta E - V_{ref} - x_1) = 0 & \text{when } s_L < 0 \\ l_2 : \left(\lambda - \frac{1}{R_0 C} \right) x_2 - \frac{1}{LC} (V_{ref} + x_1) = 0 & \text{when } s_L > 0 \end{cases} \quad (14)$$

where the lines l_1 and l_2 are the boundaries of the stable regions with the same slope $R_0/[L(\lambda R_0 C - 1)]$. And according to the two cases $0 < \lambda < 1/R_0 C$ and $\lambda > 1/R_0 C$, the stable working areas can be derived from (14) as the following Figure 2.

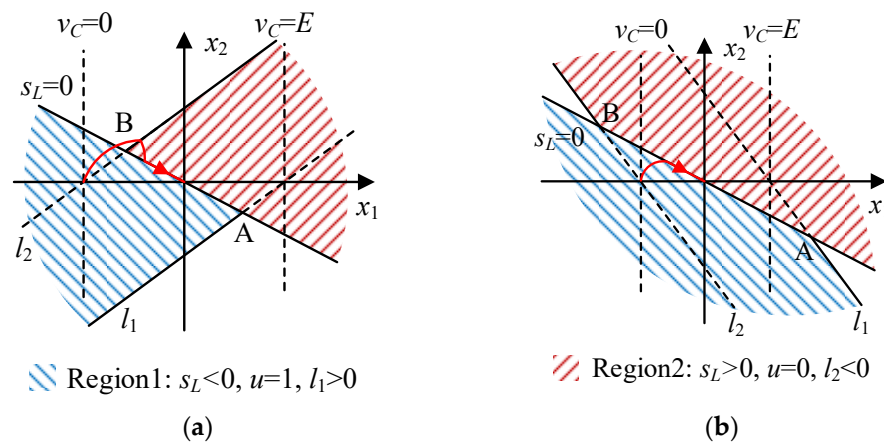


Figure 2. The stability regions of SM-controlled buck converter: (a) $\lambda > 1/R_0 C$; and (b) $0 < \lambda < 1/R_0 C$.

From (14) and Figure 2, we can see that the control performance of the system is affected by the parameters λ . Generally, the design of the SM controller in the time domain is merely based on stability. Restricted by the stability condition (14), we can see from Figure 2 that, as the output voltage v_C varies from 0 to the given value E , the system phase trajectory can only navigate between the two dashed lines l_1 and l_2 , where the intersections of two lines with $s_L = 0$ are defined as A and B, respectively. In other words, only when the phase trajectory reaches the sliding surface between points A and B, can the system stability be guaranteed.

In practice, the controller parameter λ is typically selected as the critical value $1/R_0 C$, seen in [15]. Meanwhile, the influence of the Hall sensor is often ignored. Therefore, in the following, we consider the signal loss in the transmission process of the Hall sensor to investigate its influence on the system performance in the frequency domain.

3. Design of SM Controller in Frequency Domain

Differing from the traditional design of the SM controller in the time domain, seen in Figure 2, we give the alternative controller design in the frequency domain for comparison. In the following, we still temporarily assume the transmission characteristics of the Hall sensor are ideal as the traditional time-domain SM controller in (13), i.e., $x_2 = \hat{x}_2$. For the switching control law in (11), we introduce a virtual control v as

$$v = u - 0.5 = -0.5\text{sgn}(s_L) \tag{15}$$

By substituting (15) into (4), we can obtain

$$\dot{x} = Ax + bv + f_v \tag{16}$$

where the matrix $f_v = [0, (\beta E - 2V_{ref}) / (2LC)]^T$. Therefore, if we temporarily ignore the Hall sensor, the closed-loop block diagram of the SM-controlled buck converter can be obtained by combining (10), (15), and (16), as in Figure 3, where $\sigma = -s_L$, the variable y is defined to represent the SM variable s_L , $N(A)$ is the descriptive function of the nonlinear unit (15), and $G(s)$ represents the transfer function of the linear unit of the buck converter (16) and SM surface s_L .

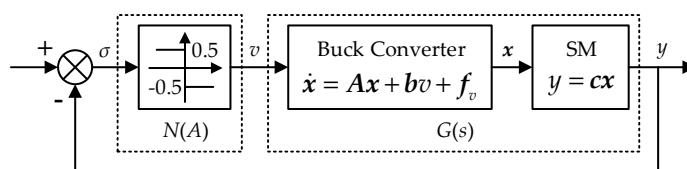


Figure 3. The closed-loop block diagram of SM-controlled buck converter without the Hall sensor.

In order to realize the controller design in the frequency domain, it is worth noticing the fact that the SM controller is inherently nonlinear due to the contained switching control law in (15). Therefore, DF is introduced in the following to realize the approximate linearization of the switching function $\text{sgn}(\cdot)$.

Based on the application of DF [24–26], it is assumed that the input of the nonlinear unit $\sigma(t)$ is a sinusoidal signal $A\sin(\omega t)$, with A and ω as the amplitude and angular frequency, respectively. By utilizing the Fourier transform for the nonlinear unit v in (15), we can obtain

$$v(t) = \frac{a_0}{2} + a_1 \cos(\omega t) + b_1 \sin(\omega t) \tag{17}$$

where a_0, a_1 , and b_1 are the corresponding coefficients of the Fourier series. Since the relay function $\text{sgn}(\cdot)$ is odd, there is $a_0 = a_1 = 0$ so that (17) can be changed as

$$v(t) = b_1 \sin(\omega t) \tag{18}$$

Here we define

$$\begin{cases} b_1 = \frac{\omega}{\pi} \int_{-\frac{\pi}{\omega}}^{\frac{\pi}{\omega}} v(t) \sin \omega t dt = -\frac{2}{\pi} \\ B = \sqrt{a_1^2 + b_1^2} = \frac{2}{\pi} \\ \varphi = \arctan \frac{a_1}{b_1} = 0 \end{cases} \tag{19}$$

Therefore, the DF of the switching control law v in (15) can be deduced from [24–26] as

$$N(A) = \frac{B}{A} e^{j\varphi} = \frac{2}{\pi A} \tag{20}$$

and the transfer function of the linear unit of buck converter (16) can also be deduced from (16) as

$$G(s) = c(Is - A)^{-1}b = \beta ER_O \frac{s+\lambda}{R_O LCs^2 + Ls + R_O} \tag{21}$$

In the frequency domain, the stability of the closed-loop control system in Figure 3 should be satisfied by the Nyquist stability criterion. Furthermore, by substituting $j\omega$ with s in (21), we can obtain

$$G(j\omega) = \beta ER_O \left[\frac{\lambda R_O - \lambda R_O LC\omega^2 + L\omega^2}{(R_O - R_O LC\omega^2)^2 + L^2\omega^2} + j \frac{-\omega^3 R_O LC + \omega R_O - \omega \lambda L}{(R_O - \omega^2 R_O LC)^2 + \omega^2 L^2} \right] \tag{22}$$

Based on the Nyquist stability criterion, it is known that the system stability is determined by the relationship of $G(j\omega)$ and $-1/N(A)$, where the three types can be seen in Figure 4. In other words, the system is stable when the trajectory of the linear part $G(j\omega)$ does not enclose the trajectory of $-1/N(A)$, and conversely, it is unstable. For the third case, self-excited oscillation will occur when the trajectory of $G(j\omega)$ intersects with $-1/N(A)$.

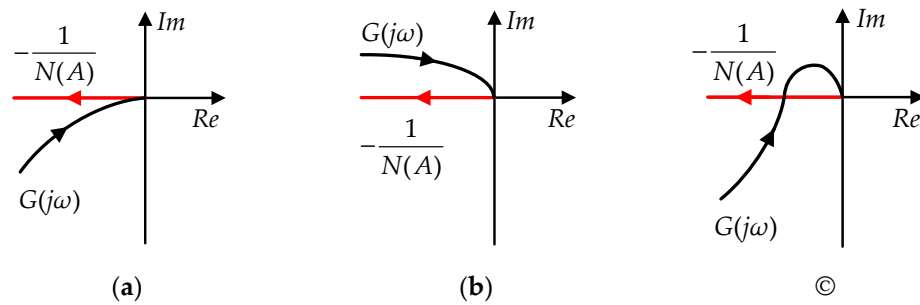


Figure 4. Three typical relationships between $G(j\omega)$ and $-1/N(A)$: (a) the trajectory of $G(j\omega)$ does not enclose $-1/N(A)$; (b) the trajectory of $G(j\omega)$ encloses $-1/N(A)$; and (c) the trajectory of $G(j\omega)$ intersects with $-1/N(A)$.

From (20), it is obvious that $-1/N(A)$ exists on the negative real axis and the system stability is determined by the intersection point of $G(j\omega)$. Furthermore, let the imaginary part of the transfer function $G(j\omega)$ be equal to zero; we can obtain $-\omega^3 R_O LC + \omega R_O - \omega \lambda L = 0$. Since the angular frequency satisfies $\omega > 0$, the solution ω_0 can be deduced as

$$\omega_0 = \sqrt{\frac{R_O - \lambda L}{R_O LC}} \tag{23}$$

From the above time-domain SM controller design in Figure 2, we can see that the controller parameters can be chosen as $\lambda \geq R_O/L$ and $0 < \lambda < R_O/L$ simultaneously. Therefore, by the frequency-domain analysis in Figure 4, the following conclusion can be obtained:

- For the case of $\lambda \geq R_O/L$, (23) has an imaginary root and there is no intersection point for the trajectory $G(j\omega)$ and the real axis, which means the system can be kept stable;
- For the case of $0 < \lambda < R_O/L$, we substitute (23) into (22) and the intersection point of the trajectory $G(j\omega)$ and the real axis can be calculated as $(\beta ER_O/L, 0)$, which indicates that $G(j\omega)$ does not intersect with the negative real axis and the system can also be kept stable.

Based on the above analysis, we can conclude that, if we ignore the influence of unmodeled dynamics of the Hall sensor, the design of the SM controller in the time domain and frequency domain is the same for the choice of controller parameter λ in (10).

4. Influence of the Unmodeled Dynamics of Hall Sensor

In the following, we continue to investigate the influence of the unmodeled dynamics of the Hall sensor. By combining (9) and (16), the unified model of the whole closed-loop control system in Figure 1 can be obtained as

$$\dot{x}_s = A_s x_s + b_s v + f_s \tag{24}$$

where the state vector $x_s = [x_1, x_2, \hat{x}_2, \dot{\hat{x}}_2]^T$, and the matrix A_s , b_s , and f_s are listed as

$$A_s = \begin{bmatrix} 0 & 1 & 0 & 0 \\ \frac{-1}{LC} & \frac{-1}{R_0 C} & 0 & 0 \\ 0 & 0 & 0 & 1 \\ 0 & K\omega_n^2 & -\omega_n^2 & -2\zeta\omega_n \end{bmatrix}, b_s = \begin{bmatrix} 0 \\ \frac{\beta E}{LC} \\ 0 \\ 0 \end{bmatrix}, f_s = \begin{bmatrix} 0 \\ \frac{\beta E}{2LC} - \frac{V_{ref}}{LC} \\ 0 \\ 0 \end{bmatrix}$$

By using DF, the corresponding closed-loop block diagram of the SM-controlled buck converter can be similarly obtained in Figure 3 as the following Figure 5, where $c_s = [\lambda, 0, 1, 0]$, $G_s(s)$ is the transfer function of the system (24).

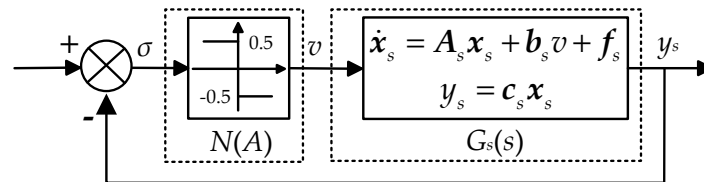


Figure 5. The closed-loop block diagram of SM-controlled buck converter with the Hall sensor.

By combining (4) with (24) and Figure 3 with Figure 5, we can see that the insertion of the Hall sensor in (5) increases the converter system order from 2 to 4, which would inevitably destroy the control performance, or even the system stability. Therefore, it is necessary to investigate the influence of the unmodeled dynamics of the Hall sensor.

4.1. Stability Analysis

From (24), the transfer function $G_s(s)$ can be deduced as

$$G_s(s) = c_s (I_s - A_s)^{-1} b_s = \beta E R_0 \frac{a_1 s^2 + a_2 s + a_3}{b_1 s^4 + b_2 s^3 + b_3 s^2 + b_4 s + b_5} \tag{25}$$

where $a_1 = \lambda$, $a_2 = (K\omega_n^2 + 2\lambda\zeta\omega_n)$, $a_3 = \lambda\omega_n^2$, $b_1 = R_0 LC$, $b_4 = (\omega_n^2 L + 2\zeta\omega_n R_0)$, $b_2 = (2\zeta\omega_n R_0 LC + L)$, $b_3 = (\omega_n^2 R_0 LC + 2\zeta\omega_n L + R_0)$, and $b_5 = \omega_n^2 R_0$.

Furthermore, by substituting $s = j\omega$ into (25), there is

$$G_s(j\omega) = \beta E R_0 [A_1 \omega^6 + A_2 \omega^4 + A_3 \omega^2 + A_4 + j(A_5 \omega^5 + A_6 \omega^3 + A_7 \omega)] / [(b_1 \omega^4 - b_3 \omega^2 + b_5)^2 + (b_2 \omega^3 - b_4 \omega)^2] \tag{26}$$

where $A_1 = -a_1 b_1$, $A_2 = a_3 b_1 + a_1 b_3 - a_2 b_2$, $A_3 = a_2 b_4 - a_3 b_3 - a_1 b_5$, $A_4 = a_1 b_4 + a_3 b_2 - a_2 b_3$, $A_5 = a_2 b_1 - a_1 b_2$, $A_6 = a_3 b_5$, and $A_7 = a_2 b_5 - a_3 b_4$.

In the sense of the Nyquist stability criterion, the influence of the Hall sensor on the system stability in Figure 5 is investigated in the frequency domain. Similar to Figure 3, the system stability is determined by the relationship of $G_s(s)$ and $-1/N(A)$ in (20). Observed from (26), since its denominator is always positive, the intersection of $G_s(j\omega)$ with the real axis leads to the following equation:

$$A_5 \omega^5 + A_6 \omega^3 + A_7 \omega = 0 \tag{27}$$

Since the angular frequency ω is typically positive, excluding the scenario with $\omega = 0$, the solution of (27) can further be deduced from Vieta’s theorem as

$$\begin{cases} \omega_1 = \sqrt{\frac{R_O - \lambda L}{R_O LC}} \\ \omega_2 = \sqrt{\frac{\omega_n^4 R_O C (KR_O - \lambda L)}{(R_O - \lambda L)(K\omega_n^2 R_O C - \lambda)}} \end{cases} \tag{28}$$

By comparing (23) and (28), we can see the stability influence imposed by the Hall sensor is determined by ω_2 in (28). According to the application of the Hall sensor, the linear types of ACS712, ACS706, and ACS758 are generally adopted [37]. Therefore, considering the signal loss in the Hall sensor, its transmission characteristic property can be described as $\hat{i}_C = Ki_C$. It implies that K is approximately equivalent to the Hall sensor’s linear amplification factor, where K can be determined by the external auxiliary circuit, seen for example in [38] for the Hall sensor of ACS712. Meanwhile, since $\hat{i}_C \cong i_C$ in practice, it means $K \cong 1$. Therefore, by substituting $K \cong 1$ into ω_2 in (28), it approximately yields

$$\omega_2 \cong \sqrt{\frac{\omega_n^4 R_O C}{\omega_n^2 R_O C - \lambda}} \tag{29}$$

Furthermore, for the rise time ψ in (8), it is equal to the following form as

$$\omega_n = \frac{\pi - \arccos\zeta}{\psi\sqrt{1 - \zeta^2}} \tag{30}$$

It should be noted that the reason for the the rise time ψ of the Hall sensor is mainly because the sensor’s dynamic performance is predominantly influenced by ψ , which is a crucial parameter. Furthermore, the rise time ψ depends particularly on the adjustment of the filter capacitance of the auxiliary circuit in typical application systems, seen for example in [39] for the Hall sensor of ACS712.

From (29) and (30), we can see that ω_2 is determined by the parameters of the SM controller λ and the Hall sensor’s rise time ψ simultaneously. Consequently, the stability of the system depends on the two parameters, so the following two cases need to be discussed.

- **Case 1:** If $\lambda > \omega_n^2 R_O C$, ω_2 is an imaginary root. Since there is no intersection point for the trajectory of $G_s(s)$ and the negative real axis, the system still keeps stable even with the consideration of the Hall sensor.
- **Case 2:** If $0 < \lambda < \omega_n^2 R_O C$, ω_2 is a real root. By substituting (27) into (24), the intersection for the trajectory of $G_s(s)$ and the real axis can be deduced as

$$G_s(j\omega_2) = -\beta ER_O \frac{\zeta\omega_n R_O C + \lambda R_O C}{2\zeta^2 R_O LC(\omega_n^2 R_O C - \lambda) + 2\zeta^2 L} \tag{31}$$

Since $0 < \lambda < \omega_n^2 R_O C$, $G_s(j\omega_2)$ yields a negative value. This means that there exists an intersection between $G_s(s)$ and $-1/N(A)$ and the whole system with the Hall sensor in (24) is critically stable, or in other words, the harmonics are contained due to the consideration of the Hall sensor.

4.2. Harmonic Analysis Affected by Hall Sensor

In the following, we continue to investigate the influence of unmodeled dynamics of the Hall sensor and further determine the relationship between the amplitude-frequency characteristics of the output signal and the Hall sensor.

From (29), since ω_2 in (29) is the solution of (31), it corresponds to the angular frequency of the harmonics, i.e., the harmonic frequency can be denoted as $f_2 = \omega_2/2\pi$. Here we define a variable $\chi = (\pi - \arccos\zeta)/(1 - \zeta^2)^{1/2}$ so that (30) can be changed as

$$\omega_n = \frac{\chi}{\psi} \quad (32)$$

By substituting (32) into (29), the relationship between the harmonic frequency f_2 and the rise time ψ of the Hall sensor can be formulated as

$$f_2 = \frac{1}{2\pi\psi} \left(\frac{\chi^4 R_O C}{\chi^2 R_O C - \lambda\psi^2} \right)^{1/2} \quad (33)$$

In accordance with the Nyquist stability criterion, $G_s(j\omega_2)$ in (31) can be evaluated by setting $G_s(j\omega) + 1/N(A) = 0$. From (20), we can have $-1/N(A) = -\pi A/2$ so that the relationship between the harmonic amplitude A_2 and the rising time ψ can be determined as

$$A_2 = \frac{\beta E R_O^2 C (\zeta\chi\psi + \lambda\psi^2)}{\pi\zeta^2 R_O^2 L C^2 \chi^2 - \pi\zeta^2 \psi^2 L (\lambda R_O C - 1)} \quad (34)$$

It is worth noticing that the buck converter is assumed to work in CCM, as seen in (1). In other words, if the induct current i_L is assumed to be critical continuous, the current harmonics ΔI_L in a switching period T can be expressed from [39] as

$$\Delta I_L = \left| \frac{1}{L} \int_0^{DT} v_L dt \right| = \frac{V_C}{E L f_{2\min}} (E - V_C) = \frac{2V_C}{R_O} \quad (35)$$

where $f_{2\min}$ is the minimum value of the harmonic frequency f_2 in (33), V_C is the average value of the output voltage v_c in a switch period T , and D represents the duty cycle with $D = V_C/E$. Therefore, the critical value of the switching frequency f_m is deduced from [39] as

$$f_m = \frac{(E - V_C) R_O}{2EL} \quad (36)$$

Since the switching frequency is proportional to the harmonic frequency of the system, it means the switching frequency f_m in (36) corresponds to the minimum value of the harmonic frequency $f_{2\min}$. Hence, the constraint $f_2 \geq f_m$ should be guaranteed. Therefore, by combining (33) and (36), the rising time ψ of the Hall sensor can be deduced as

$$0 < \psi \leq \frac{EL}{\pi(E - V_C) R_O} \left(\frac{\chi^4 R_O C}{\chi^2 R_O C - \lambda\psi^2} \right)^{1/2} \quad (37)$$

which is helpful for the choice of the Hall sensor.

Based on the above analysis concerning the SM controller parameter λ and the rise time ψ of the Hall sensor, we conclude the following:

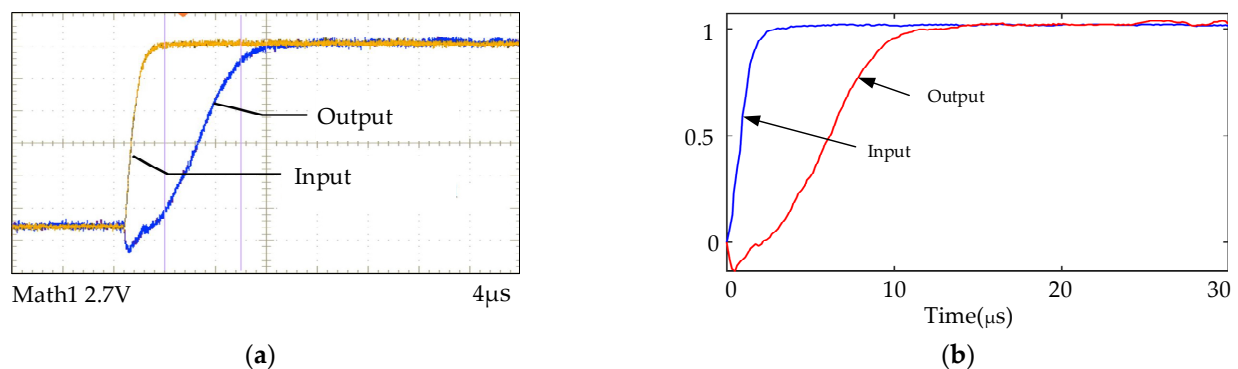
- If the SM controller parameter $\lambda > \omega_n^2 R_O C$, the whole closed-loop control system of the SM-controlled buck converter system has no harmonics;
- If the SM controller parameter $0 < \lambda < \omega_n^2 R_O C$, the constraint of the harmonic frequency $f_2 \geq f_m$ can be deduced, and the rising time ψ of the Hall sensor can also be obtained, which gives guidance to the choice of SM parameter λ and the Hall sensor in practical systems.

5. Simulations and Experiments

In order to validate this paper, the circuit parameters of the buck converter in Figure 1 are listed in Table 1. The Hall sensor of ACS 712 is chosen, where the measurement characteristics in its chip manual [40] and the corresponding fitting model based on the collected data can be seen in Figure 6.

Table 1. Circuit Parameters of the Buck Converter.

Component	Symbol	Value
Input voltage	E	20 V
Inductor	L	1 mH
Capacitor	C	3.2 mF
Load resistor	R	10 Ω
Divider resistor 1	R_1	10,000 Ω
Divider resistor 2	R_2	50,000 Ω
Reference output voltage	V_{ref}/β	10 V

**Figure 6.** Characteristic curve of Hall sensor ACS712: (a) the test data in chip manual; and (b) the fitting model based on the collected data.

In Figure 6b, we utilize the GetData software to collect the test data of the chip ACS712 in the datasheet, and then using MATLAB's Identification Toolbox, the unmodeled dynamics of the Hall sensor in (6) can be described as

$$G_h(s) = \frac{2.235 \times 10^{11}}{s^2 + 6.691 \times 10^5 s + 2.251 \times 10^{11}} \quad (38)$$

By comparing (6) and (38), we can deduce the amplification coefficient $K = 0.993$, not the ideal 1, which indicates the signal loss of the real sensor ACS712 is included. The damping ratio $\zeta = 0.705$, and the angular frequency $\omega_n = 4.744 \times 10^5$.

5.1. Simulation Results

In the following, we test the influences of the unmodeled dynamics of the Hall sensor and SM controller parameter λ on the buck converter system simultaneously. In order to facilitate the expatiation, we abbreviate the model of the buck converter without consideration of the Hall sensor in (4) as the 'ideal system', and the model with the Hall sensor in (24) as the "actual system".

Firstly, we investigate the influence of the unmodeled dynamics of the Hall sensor on the system. The rise time of the Hall sensor ACS712 is chosen as $\psi = 6.647 \mu\text{s}$ and the angular frequency calculated from (30) as $\omega_n = 4.992 \times 10^5$. For the SM controller parameter λ , the traditional time-domain design approach in Section 2.3 differs from the frequency-domain design approach. For the former, it is based on the model of the ideal system with the SM controller parameter $\lambda > 1/R_0C$ and $0 < \lambda < 1/R_0C$, seen in Figure 2. While for the actual system with consideration of the Hall sensor, the stability region without harmonics is deduced as $\lambda > \omega_n^2 R_0C$, seen from (29). Since there is $1/R_0C = 31.25$ and $\omega_n^2 R_0C = 7.973 \times 10^9$, we select SM parameters $\lambda_1 = 31.25$ for the ideal system and $\lambda_2 = 8 \times 10^9$ for the actual system for comparison. Simulation results are given in Figures 7 and 8.

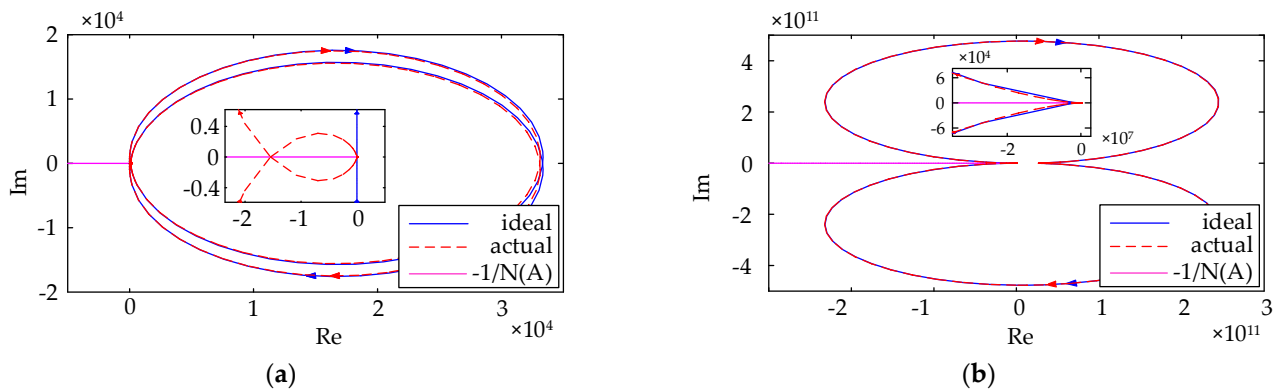


Figure 7. Nyquist curves with different parameter λ : (a) $\lambda_1 = 31.25$; and (b) $\lambda_2 = 8 \times 10^9$.

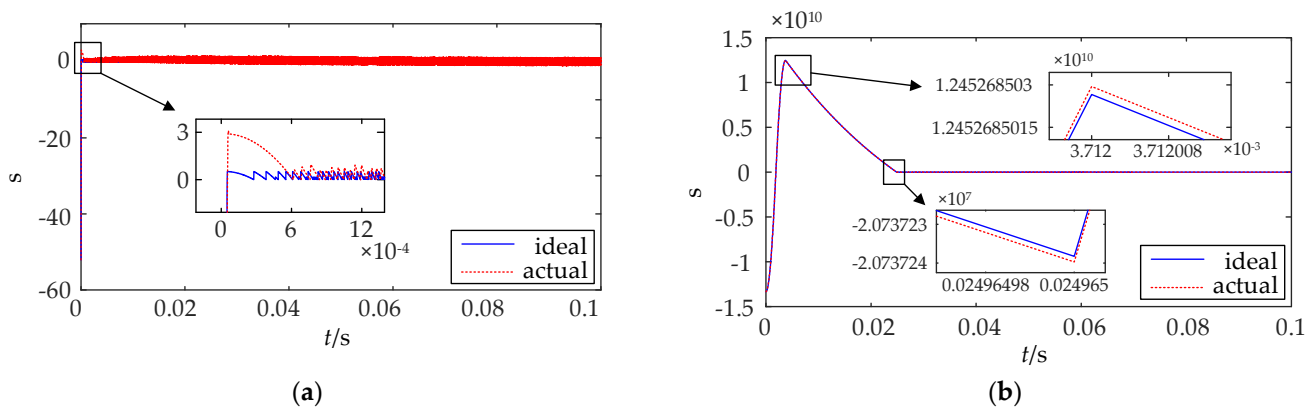


Figure 8. Time-domain response curve of the SM surface with different parameter λ : (a) $\lambda_1 = 31.25$; and (b) $\lambda_2 = 8 \times 10^9$.

For the SM controller parameter $\lambda_1 = 31.25 < \omega_n^2 R_0 C$, Figure 7a shows that the Nyquist curve $G(j\omega)$ of the ideal system defined in (22), which neither encloses nor intersects with the line of $-1/N(A)$ defined in (20). However, for the Nyquist curve $G_s(j\omega)$ of the actual system defined in (31), corresponds to the scenario in Figure 4c, which means the existence of an intersection point for the Nyquist curve $G_s(j\omega)$ with the line of $-1/N(A)$. Since the line of $-1/N(A)$ passes from an enclosed region of $G_s(j\omega)$ to an unenclosed region, stable self-oscillation occurs, which is just the reason for the occurrence of the harmonic problem. On the other hand, if the SM controller parameter is chosen $\lambda_2 = 8 \times 10^9 > \omega_n^2 R_0 C$, similarly Figure 7b gives the comparison of the Nyquist curves for the ideal system and the actual system. We can see that neither $G(j\omega)$ for the ideal system nor $G_s(j\omega)$ for the actual system encloses the line of $-1/N(A)$, which is in accordance with the scenario in Figure 4a.

Figure 8 shows the time-domain response curve of the SM surface s_L defined in (10). For the case with $\lambda_1 = 31.25$ in Figure 8a, we can see the ideal system and the actual system can both keep stable, but there exists an overshoot for the latter, which is caused by the insertion of the unmodeled dynamics of the Hall sensor in (38), which makes the system order increase from 2 to 4. This is in accordance with the explanation in (31). Figure 8b shows the comparison in the case with $\lambda_2 = 8 \times 10^9$. As mentioned in Figure 6b, it corresponds to the situation without consideration of the Hall sensor, so that the response curves of the ideal and actual system are almost the same and no harmonics occur.

In the following, we continue to investigate the influence of the SM controller parameter λ on the actual system by choosing $\lambda_1 = 31.25$, $\lambda_2 = 10^3$, $\lambda_3 = 10^5$, $\lambda_4 = 8 \times 10^9$, and $\lambda_5 = 9 \times 10^9$ for performance comparison. The simulations concerning the inductor current i_L and the output voltage v_c are given in Figure 8.

From Figure 9a,b, we can see harmonics occur in both the inductor current i_L and the output voltage v_c in cases of $\lambda_1 = 31.25$, $\lambda_2 = 10^3$, and $\lambda_3 = 10^5$, while for the other cases of $\lambda_4 = 8 \times 10^9$ and $\lambda_5 = 9 \times 10^9$, there are no harmonics. This is in accordance with the theoretical analysis in (30). The values of the amplitude and frequency for the cases with $\lambda_1 = 31.25$, $\lambda_2 = 10^3$, and $\lambda_3 = 10^5$ are listed as 1.6×10^{-5} V and 78.74 kHz, 1.6×10^{-5} V and 78.77 kHz, and 1.6×10^{-5} V and 78.77 kHz. In the premise of system stability, we can see that the different values of the SM controller parameter λ have less influence on the amplitude-frequency characteristics of the buck converter system with the Hall sensor.

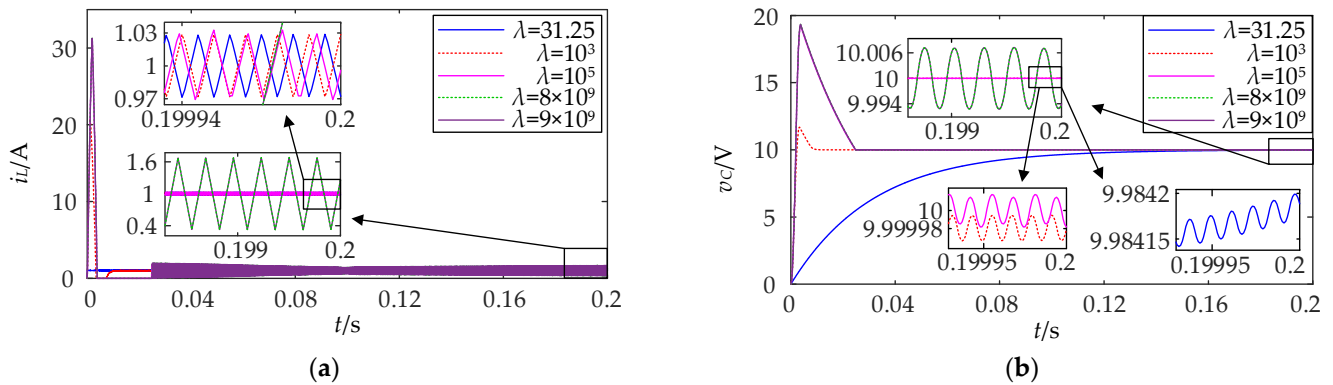


Figure 9. Performance influence of SM parameter λ : (a) inductor current i_L ; and (b) output voltage v_c .

Thirdly, we investigate the influence of the rising time ψ of the Hall sensor on the system performances. According to the datasheet of ACS712 [40], we choose five values of $\psi = 6.647 \mu\text{s}$, $32.09 \mu\text{s}$, $88.18 \mu\text{s}$, $211.3 \mu\text{s}$, and $291.26 \mu\text{s}$ for comparison. The simulations are given in Figure 10 and Table 2.

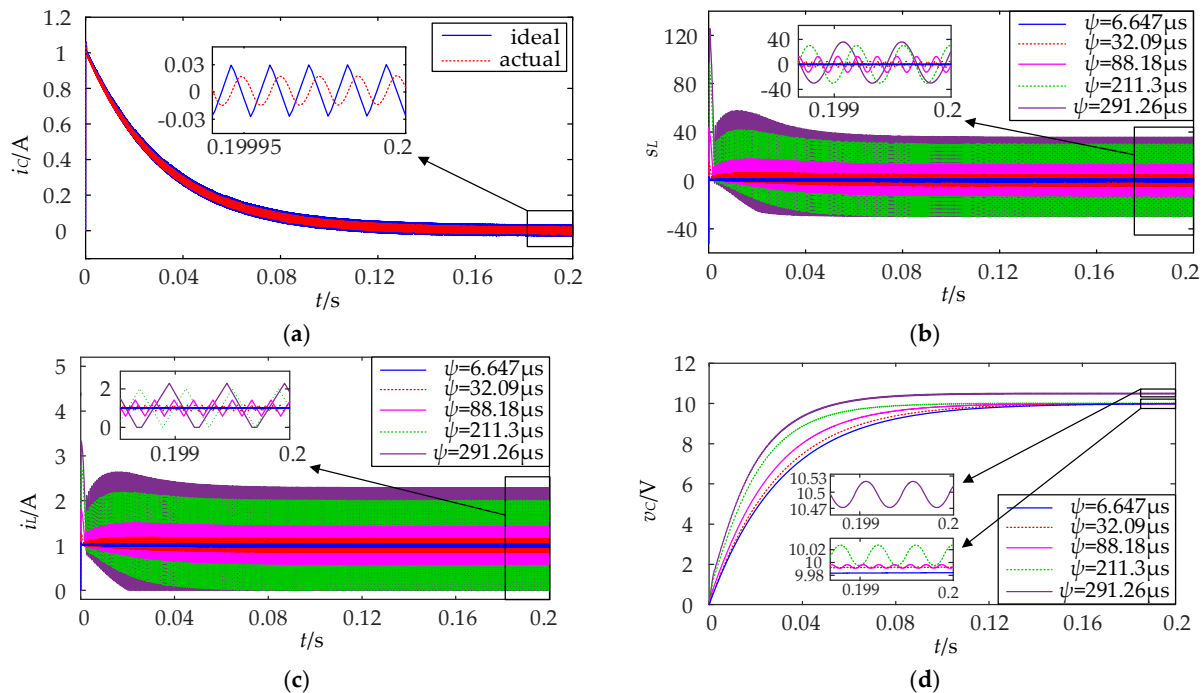


Figure 10. Performance influence of Hall sensor parameter ψ : (a) capacitor current i_C ; (b) sliding variable s_L ; (c) inductor current i_L ; and (d) output voltage v_c .

Table 2. Comparison of the Output Voltage with Varying ψ .

Rise Time ψ (μs)	Theoretical Value of Harmonic Amplitude A_2 (mV)	Simulation Value of Harmonic Amplitude A_2 (mV)	Theoretical Value of Harmonic Frequency f_2 (kHz)	Simulation Value of Harmonic Frequency f_2 (kHz)	Steady Error of Output Voltage v_C (mV)
6.647	0.94	0.96	79.45	78.74	0.032
32.09	4.55	4.62	16.46	16.18	0.741
88.18	12.51	12.67	5.99	5.88	5.59
211.3	30.03	29.99	2.50	2.50	31.3
291.26	41.44	32.99	1.81	1.99	48.6

From Figure 10, we can see that the influence of the unmodeled dynamics of the Hall sensor cannot be ignored, despite the small value of the rising time ψ in the grade of μs . As observed from Table 2, as the increase of the rise time ψ , the frequency of the harmonics will decrease, while the amplitude and the steady error will increase. It is worth noticing that, if $\psi = 211.3 \mu\text{s}$, it corresponds to the maximum value to keep the buck converter working in CCM based on the data sheet of ACS 712 in [40] and (36), (37). Therefore, if $\psi = 291.26 \mu\text{s}$, the inductor current i_L is discontinuous, which can degrade the control performance and increase the steady error, as seen in Table 2.

5.2. Experimental Results

In the following, we further test the influence of the unmodeled dynamics of the Hall sensor by experiment. In Figure 11, the experiment platform based on DSpace 1106 is given, where the sampling time is 0.5 ms and the PWM frequency is 10 k0 Hz. In Figure 12a, the hardware of the buck converter is given, and in Figure 12b, the circuit of the contained Hall sensor ACS712 is given, where the five chosen values 6.647 μs , 32.09 μs , 88.18 μs , 211.3 μs , and 291.26 μs of the rise times ψ in Figure 10 and Table 2 can be obtained by adjusting the capacitor C_F on the basis of its chip manual [40].

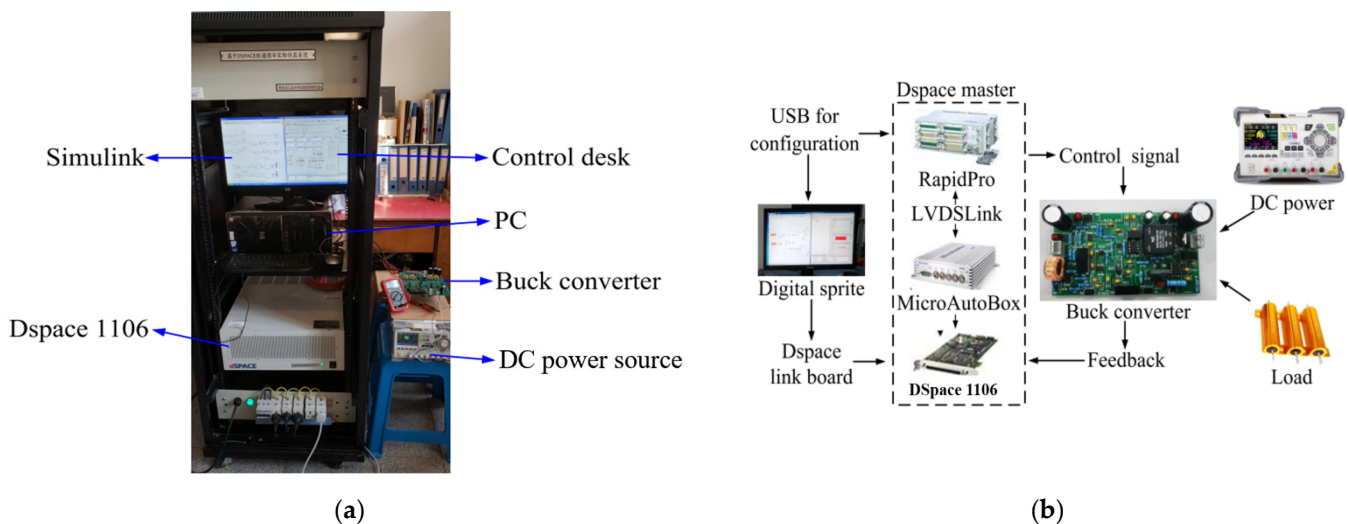
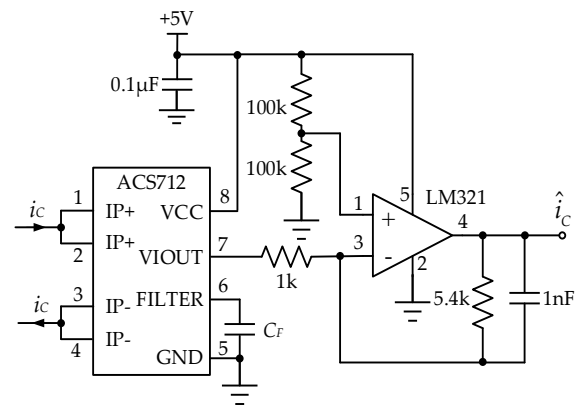


Figure 11. dSPACE experiment platform of buck converter system:(a) platform of DSpace 1106; (b) connection diagram of the platform.



Hall sensor ACS712

(a)



(b)

Figure 12. Hardware of buck converter with Hall sensor ACS712: (a) hardware; and (b) circuit of Hall sensor ACS712.

Based on the chip manual of the Hall sensor ACS712 in [40], we focus on investigating the main issue of this paper, i.e., the influence of the unmodeled dynamics of the Hall sensor on the control performance of the SM-controlled buck converter system in Figure 1. Here we let the SM controller parameter be $\lambda = 31.25$ and vary the rise time ψ as $6.647 \mu\text{s}$, $32.09 \mu\text{s}$, $88.18 \mu\text{s}$, $211.3 \mu\text{s}$, and $291.26 \mu\text{s}$, where the corresponding values of the capacitor C_F can be seen in Table 3. The experimental results are given in Figure 13 and Table 3. We can see that, as the rise time ψ increases from $6.647 \mu\text{s}$ to $291.26 \mu\text{s}$, the steady-state error of the output voltage v_C increases from 12.3 mV to 103.7 mV , and the harmonic amplitudes vary from 428 mV to 812 mV . Therefore, it proves the influence of the Hall sensor cannot be ignored.

Table 3. Comparisons of the Output Voltage with Varying ψ .

Rise Time ψ (μs)	Adjusted Capacitor C_F (nF)	Harmonic Amplitude A_2 (mV)	Steady Error of Output Voltage v_C (mV)
6.647	0	428	12.3
32.09	10	528	26.1
88.18	47	568	50.1
211.3	70	688	83.4
291.26	100	812	103.7

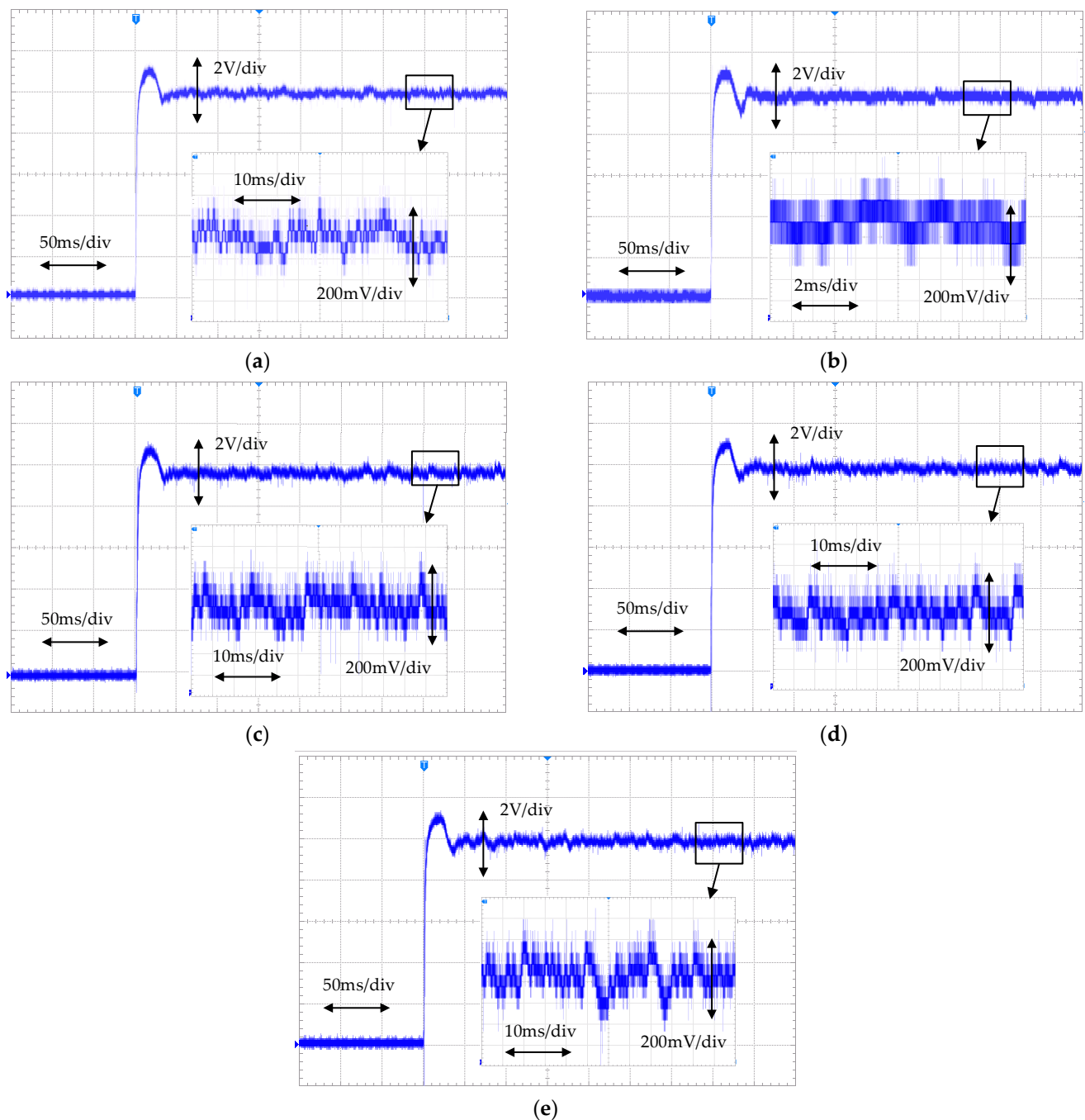


Figure 13. Experimental results affected by the unmodeled dynamics of Hall sensor ACS712: (a) $\psi = 6.647 \mu\text{s}$, $C_F = 0 \text{ nF}$; (b) $\psi = 32.09 \mu\text{s}$, $C_F = 10 \text{ nF}$; (c) $\psi = 88.18 \mu\text{s}$, $C_F = 47 \text{ nF}$; and (d) $\psi = 211.3 \mu\text{s}$, $C_F = 70 \text{ nF}$; (e) $\psi = 291.26 \mu\text{s}$, $C_F = 100 \text{ nF}$.

6. Conclusions

In this paper, we investigate the harmonic problem of SM-controlled buck converters imposed by the often-ignored unmodeled dynamics of the Hall sensor. The advantages of this paper lies on the following three points:

- The unmodelled dynamics of the Hall sensor are included into the modelling of the SM-controlled converter system, and the experimental modeling approach in Figure 6 and (38) guarantees the modelling precision and accuracy;
- For the design of SM controller, this paper replaces the traditional time-domain approach based on the Lyapunov stability theorem with a frequency-domain approach

by using DF and Nyquist stability criterion, which innovatively proves the inevitable existence of harmonics caused by the unmodeled dynamics of Hall sensor;

- The quantitative relationship between the amplitude frequency characteristics of the output signal and the Hall sensor is determined, seen in (33) and (34), which gives guidance for the choice of SM parameter λ and the Hall sensor in practical systems.

At the same time, some issues concerning the limitations and potential areas for the further research should also be considered. For example:

- In this paper, the sensor unmodelled dynamics are only considered; what about other or multiple unmodelled dynamics affect the stability and control performance of the system?
- In this paper, the commonly used linear sliding mode control approach is adopted; what about other complex SM types are used for the control of buck converters?
- What is significant and valuable for the theoretical and applied research of SM-controlled buck converter systems.

Author Contributions: Conceptualization, Y.W.; methodology, Y.W. and G.D.; software, G.D., J.N. and B.L.; investigation, J.Y., writing—original draft, Y.W. and G.D.; writing—review and editing, J.Y. and W.Y.; project administration, Y.W.; experiment, G.D., J.N. and B.L. All authors have read and agreed to the published version of the manuscript.

Funding: This research is funded by the National Natural Science Foundation of China Under Grant No. 51307035, 62073095 and the Open Foundation of Anhui Province Key Laboratory of Intelligent Building & Building Energy Saving Under Grant No. IBES2021KF02.

Data Availability Statement: Not applicable.

Conflicts of Interest: The authors declare no conflict of interest.

References

1. Batarseh, I.; Alluhaybi, K. Emerging Opportunities in Distributed Power Electronics and Battery Integration: Setting the Stage for an Energy Storage Revolution. *IEEE Trans. Power Electron.* **2020**, *7*, 22–32. [[CrossRef](#)]
2. AndradeL, A.M.S.S.; Schuch, L.; Martins, M.L.D.S. Analysis and Design of High-Efficiency Hybrid High Step-Up DC–DC Converter for Distributed PV Generation Systems. *IEEE Trans. Ind. Electron.* **2019**, *66*, 3860–3868. [[CrossRef](#)]
3. Mayo-Maldonado, J.C.; Ruiz-Martinez, O.F.; Escobar, G.; Valdez-Resendiz, J.E.; Maupong, T.M.; Rosas-Caro, J.C. Nonlinear Stabilizing Control Design for DC–DC Converters Using Lifted Models. *IEEE Trans. Ind. Electron.* **2021**, *68*, 10772–10783. [[CrossRef](#)]
4. Riaz, M.; Yasin, A.; Uppal, A.; Yasin, A. A Novel Dynamic Integral Sliding Mode Control for Power Electronic Converters. *Sci. Prog.* **2021**, *104*, 00368504211044848. [[CrossRef](#)] [[PubMed](#)]
5. Wu, L.; Liu, J.; Vazquez, S.; Mazumder, S.K. Sliding Mode Control in Power Converters and Drives: A Review. *IEEE/CAA J. Autom. Sin.* **2022**, *9*, 392–406. [[CrossRef](#)]
6. Rosales, A.; Ibarra, L.; Ponce, P.; Molina, A. Fuzzy Sliding Mode Control Design Based on Stability Margins. *J. Frankl. Inst.* **2019**, *356*, 5260–5273. [[CrossRef](#)]
7. Prieto, P.J.; Cazarez-Castro, N.R.; Aguilar, L.T.; Cardenas-Maciel, S.L. Chattering Existence and Attenuation in Fuzzy-Based Sliding Mode Control. *Eng. Appl. Artif. Intell.* **2017**, *61*, 152–160. [[CrossRef](#)]
8. Zhao, Y.; Niu, B.; Wang, H.; Yang, D. Adaptive Neural Tracking Control of Nonlinear Nonstrict-Feedback Systems with Unmodeled Dynamics. *IEEE Access* **2019**, *7*, 90206–90214. [[CrossRef](#)]
9. Wang, J.; Luo, W.; Liu, J.; Wu, L. Adaptive Type-2 FNN-Based Dynamic Sliding Mode Control of DC–DC Boost Converters. *IEEE Trans. Syst. Man Cybern. Syst.* **2021**, *51*, 2246–2257. [[CrossRef](#)]
10. Gheisarnejad, M.; Farsizadeh, H.; Khooban, M.H. A Novel Nonlinear Deep Reinforcement Learning Controller for DC–DC Power Buck Converters. *IEEE Trans. Ind. Electron.* **2021**, *68*, 6849–6858. [[CrossRef](#)]
11. Zhang, L.; Wang, Z.; Li, S.; Ding, S.; Du, H. Universal Finite-Time Observer Based Second-Order Sliding Mode Control for DC-DC Buck Converters with Only Output Voltage Measurement. *J. Frankl. Inst.* **2020**, *357*, 11863–11879. [[CrossRef](#)]
12. Wu, W.; Qiu, L.; Liu, X.; Guo, F.; Rodriguez, J.; Ma, J.; Fang, Y. Data-Driven Iterative Learning Predictive Control for Power Converters. *IEEE Trans. Power Electron.* **2022**, *37*, 14028–14033. [[CrossRef](#)]
13. Shieh, H.; Chen, Y. A Sliding Surface-Regulated Current-Mode Pulse-Width Modulation Controller for a Digital Signal Processor-Based Single Ended Primary Inductor Converter-Type Power Factor Correction Rectifier. *Energies* **2017**, *10*, 1175. [[CrossRef](#)]
14. Wang, J.; Li, S.; Yang, J.; Wu, B.; Li, Q. Extended State Observer-Based Sliding Mode Control for PWM-Based DC-DC Buck Power Converter Systems with Mismatched Disturbances. *IET Control. Theory Appl.* **2015**, *9*, 579–586. [[CrossRef](#)]

15. Guo, J. Application of Full Order Sliding Mode Control Based on Different Areas Power System with Load Frequency Control. *ISA Trans.* **2019**, *92*, 23–34. [[CrossRef](#)] [[PubMed](#)]
16. Wu, L.; Mei, P.; Lei, B.; Lin, Z. Dead-Beat Terminal Sliding Mode Control with Application to DC–DC Buck Converters. *IEEE Trans. Circuits Syst. II: Express Briefs* **2023**, *70*, 2470–2474. [[CrossRef](#)]
17. Wang, Z.; Li, S.; Li, Q. Continuous Nonsingular Terminal Sliding Mode Control of DC–DC Boost Converters Subject to Time-Varying Disturbances. *IEEE Trans. Circuits Syst. II Express Briefs* **2020**, *67*, 2552–2556. [[CrossRef](#)]
18. Ni, C.J.; Liu, C.; Pang, X. Fuzzy Fast Terminal Sliding Mode Controller Using an Equivalent Control for Chaotic Oscillation in Power System. *Acta Phys. Sin.* **2013**, *62*, 190507.
19. Jiang, C.; Wang, Q.; Li, Z.; Zhang, N.; Ding, H. Nonsingular Terminal Sliding Mode Control of PMSM Based on Improved Exponential Reaching Law. *Electronics* **2021**, *10*, 1776. [[CrossRef](#)]
20. Abolvafoei, M.; Ganjefar, S. Adaptive Second-Order Terminal PID Sliding Mode Control Design for Integer-Order Approximation of Wind Turbine System for Maximum Power Extraction. *IET Control. Theory Appl.* **2021**, *15*, 2210–2220. [[CrossRef](#)]
21. Hu, R.; Deng, H.; Zhang, Y. Novel Dynamic-Sliding-Mode-Manifold-Based Continuous Fractional-Order Nonsingular Terminal Sliding Mode Control for a Class of Second-Order Nonlinear Systems. *IEEE Access* **2020**, *8*, 19820–19829. [[CrossRef](#)]
22. Bernardo, D.; Johansson, K.; Vasca, F. Self-Oscillations and Sliding in Relay Feedback Systems: Symmetry and Bifurcations. *Int. J. Bifurc. Chaos* **2021**, *11*, 1121–1140. [[CrossRef](#)]
23. Boiko, I.; Fridman, L.; Pisano, A.; Usai, E. Fast Oscillations in Feedback Control Systems with Fast Actuators Driven by the Second-Order Sliding Mode Suboptimal Algorithm. In Proceedings of the 43rd IEEE Conference on Decision and Control, SNC Lavalin, Calgary, AB, Canada, 14–17 December 2004.
24. Li, H.; Shang, J.; Zhang, B.; Zhao, X.; Tan, N.; Liu, C. Stability Analysis with Considering the Transition Interval for PWM DC-DC Converters Based on Describing Function Method. *IEEE Access* **2018**, *6*, 48113–48124. [[CrossRef](#)]
25. Inanlou, R.; Shoaie, O.; Tamaddon, M.; Rescati, M.; Baschiroto, A. Analysis and Design of an Asynchronous Pulse-Width Modulation Technique for Switch Mode Power Supply. *IET Power Electron.* **2020**, *13*, 1639–1648. [[CrossRef](#)]
26. Marquart, C.A.; Zourtos, T.; Magierowski, S.; Mathai, N.J. Sliding-Mode Amplitude Control Techniques for Harmonic Oscillators. *IEEE Trans. Circuits Syst. II Express Briefs* **2007**, *54*, 1014–1018. [[CrossRef](#)]
27. Aranya, C.; Murat, A. Robust Stabilization and Performance Recovery of Nonlinear Systems with Unmodeled Dynamics. *IEEE Trans. Autom. Control.* **2009**, *54*, 1351–1356.
28. Yan, H.; Xu, Y.; Zhao, W.; Zhang, H.; Gerada, C. DC Drift Error Mitigation Method for Three-Phase Current Reconstruction with Single Hall Current Sensor. *IEEE Trans. Magn.* **2019**, *55*, 1–4. [[CrossRef](#)]
29. Liu, C.; Liu, H.J.G. Offset Error Reduction in Open Loop Hall Effect Current Sensors Powered with Single Voltage Source. In Proceedings of the 2014 IEEE International Workshop on Applied Measurements for Power Systems Proceedings (AMPS), Aachen, Germany, 24–26 September 2014.
30. Wang, L.; Sun, Y.; Yang, L.; Lv, Y.; Tang, L. Numerical Model of Hall Sensor at the Source of a Rectangular Magnet Field. In Proceedings of the 2022 International Conference on Sensing, Measurement & Data Analytics in the Era of Artificial Intelligence (ICSMD), Harbin, China, 30 November–2 December 2022.
31. Lee, H.; Utkin, V. Chattering Suppression Methods in Sliding Mode Control Systems. *Annu. Rev. Control.* **2007**, *31*, 179–188. [[CrossRef](#)]
32. Wang, W.; Ma, J.; Li, X.; Cheng, Z.; Zhu, H.; Teo, C.S.; Lee, T.H. Iterative Super-Twisting Sliding Mode Control for Tray Indexing System with Unknown Dynamics. *IEEE Trans. Ind. Electron.* **2021**, *68*, 9855–9865. [[CrossRef](#)]
33. Si, Y.; Pu, J.; Lu, B.; Sun, L. An Improved Adaptive Neural Network Sliding Mode Method for Tracking Control. In Proceedings of the 2018 Chinese Automation Congress (CAC), Xi’an, China, 30 November–2 December 2018.
34. Alipour, M.; Zarei, J.; Razavi-Far, R.; Saif, M.; Mijatovic, N.; Dragičević, T. Observer-Based Backstepping Sliding Mode Control Design for Microgrids Feeding a Constant Power Load. *IEEE Trans. Ind. Electron.* **2023**, *70*, 465–473. [[CrossRef](#)]
35. Zhao, Z.; Gu, H.; Zhang, J.; Ding, G. Terminal Sliding Mode Control Based on Super-Twisting Algorithm. *J. Syst. Eng. Electron.* **2017**, *28*, 145–150. [[CrossRef](#)]
36. Sung, G.; Wang, W.; Yu, C. Analysis and Modeling of One-Dimensional Folded Vertical Hall Sensor with Readout Circuit. *IEEE Sens. J.* **2017**, *17*, 6880–6887. [[CrossRef](#)]
37. Ranasingh, S.; Pradhan, T.; Raju, D.; Singh, A.; Piantini, A. An Approach to Wire-Wound Hall-Effect Based Current Sensor for Offset Reduction. *IEEE Sens. J.* **2022**, *22*, 2006–2015. [[CrossRef](#)]
38. Li, L.; Chen, Y.; Zhou, H.; Ma, H.; Liu, J. The Application of Hall Sensors ACS712 in the Protection Circuit of Controller for Humanoid Robots. In Proceedings of the 2010 International Conference on Computer Application and System Modeling (ICASM 2010), Taiyuan, China, 22–24 October 2010.

39. De Gusseme, K.; Van de Sype, D.M.; Van den Bossche, A.P.; Melkebeek, J.A. Digitally Controlled Boost Power-Factor-Correction Converters Operating in Both Continuous and Discontinuous Conduction Mode. *IEEE Trans. Ind. Electron.* **2005**, *52*, 88–97. [[CrossRef](#)]
40. ACS712 Datasheet (PDF)-Allegro MicroSystems. Available online: <https://www.alldatasheet.com/datasheet-pdf/pdf/168326/ALLEGRO/ACS712.html> (accessed on 18 August 2023).

Disclaimer/Publisher’s Note: The statements, opinions and data contained in all publications are solely those of the individual author(s) and contributor(s) and not of MDPI and/or the editor(s). MDPI and/or the editor(s) disclaim responsibility for any injury to people or property resulting from any ideas, methods, instructions or products referred to in the content.